PCCP

Accepted Manuscript

ROYAL SOCIETY OF CHEMISTRY

www.rsc.org/pccp

Physical Chemistry Chemical Physics RSCPublishing

ARTICLE

Thermal and shape stability of high-index-faceted rhodium nanoparticles: a molecular dynamics investigation

Cite this: DOI: 10.1039/xoxxoooooox

Received ooth January 2014,
Accepted ooth January 2014

DOI: 10.1039/xoxxoooooox

www.rsc.org/

Xiang-Ming Zeng,[a] Rao Huang,[*,a] Yu-Hua Wen[*,a] and Shi-Gang Sun[b]

Nano-sized noble metallic particles enclosed by high-index facets exhibit superior catalytic activity because of their high density of low-coordinated step atoms at surface, thus have attracted growing interest over the past decade. In this article, we have employed molecular dynamics simulations to investigate the thermodynamic evolution of tetrahexahedral Rh nanoparticles respectively covered by {210}, {310} and {830} facets during heating process. Our results reveal that the {210} faceted nanoparticle exhibits better thermal and shape stability than the {310} and {830} faceted ones. Meanwhile, since {830} facet consists of {210} and {310} subfacets, the stability of {830} faceted Rh nanoparticle is dominated by {310} subfacet which possesses relatively poor stability. Furthermore, the shape transformation of these nanoparticles is much earlier than their melting. Further analyses indicate that surface atoms with higher coordination numbers display lower surface diffusivity, thus being helpful for stabilizing the particle shape. This study offers an atomistic understanding of thermodynamic behaviors of high-index-faceted Rh nanoparticles.

1. Introduction

Rhodium nanoparticles (NPs) have been widely used as a class of catalysts due to their excellent chemical properties, particularly in fine chemicals synthesis, automobile catalytic converters, oil refining processes, and energy conversion technology.[1-4] However, the low reserve and high cost of raw material seriously limit their further use, thus driving much research aiming to maximize their utilization efficiency.

Because catalytic reactions usually occur on the surface of NPs, the catalytic properties of NPs are strongly dependent not only on the particle sizes but also on the particle shapes which are defined by the crystallographic orientation of the surface.[5-9] Fundamental studies on fcc metallic single-crystal surfaces have demonstrated that high-index planes exhibit much higher reactivity than low-index ones such as {111} and {100} because they have a large density of low-coordinated atoms situated on steps, ledges and kinks which usually serve as the active sites.[10,11] Therefore, Shape- and size-controlled syntheses of NPs are of considerable significance for tuning their catalytic activity and selectivity. However, it is greatly challenging to synthesize high-index-faceted NPs because the high-index planes would be preferentially eliminated during fabrication process due to the fact that thermodynamics of crystallization commonly requires the minimization of the total surface energy.[12] A breakthrough progress has been achieved by Sun *et al.* who have successfully synthesized tetrahexahedral (THH) Pt NPs enclosed by {730} and vicinal high-index facets in 2007.[13] Since then, extensive studies have been devoted to preparing high-index-faceted metallic NPs. Resultantly, a variety of noble metallic (Pt, Pd, Au) polyhedral NPs bound by high-index-facets have been synthesized in the following years.[14-19] It should be pointed out that there are few reports on the synthesis of Rh NPs with high-index facets because of the extraordinary high surface energy of Rh in comparison with other noble metals such as Pt, Pd, Au. To date, most of synthesized Rh NPs are covered by low-index facets such as {111} and {100}.[20-23] It is worthy noting that, very recently, Sun *et.al* successfully prepared THH Rh NPs with {830} facets by employing the electrochemical square-wave potential method.[24] As was expected, these high-index-faceted Rh NPs exhibited much higher catalytic activity for the electrooxidation of ethanol and CO than commercial Rh catalysts.[24]

Although the high-index facets of Rh NPs are beneficial to enhancing the catalytic performance, their stability will be compromised at the same time owing to their high surface energy. As we know, the thermal stability of Rh NPs is of importance for

their syntheses and applications. On one hand, the NPs tend to aggregate into larger particles due to the enhanced atomic diffusion at the ambient temperature close to the Tammann temperature.[25] Therefore, to control the synthesis and the operation temperature reasonably is of technological significance for suppressing their sintering and coarsening. On the other hand, a large number of catalytic reactions are high-temperature involved, especially in the cracking of petroleum and the purification of automobile exhaust gases. Since these reactions preferentially take place on surfaces,[26] the high-index facets are easily destroyed in these situations, and the excellent catalytic properties of these NPs will be lost. Hence, an in-depth understanding of thermal and shape stability is crucial for stabilizing particle shape and surface structure of Rh NPs at elevated temperatures.

In this article, THH Rh NPs bound by different high-index facets were addressed. These NPs were continuously heated to examine their thermal and shape stability by means of atomistic simulations. Both the microstructural and shape evolution of the NPs during the heating process were explored. To our knowledge, this is the first report on the thermodynamic stability of polyhedral Rh nanoparticles. This article is structured as follows. Section 2 briefly describes the simulation methods. Section 3 presents the calculated results, discussion and comparison with available results. The main conclusions are summarized in the fourth section.

2. Simulation Methodology

As is known, the THH NPs are enclosed by twenty-four facets of Miller indices {*hk*0} with at least one index being larger than unit.[26] The tetrahexahedron can be considered as a cube with each face capped by a square pyramid (see Fig. 1a). Fig. 1b and 1c respectively illustrate the atomic arrangement of THH NP and the {830} high-index plane enclosing the particle. Note that the {830} surface is periodically composed of one {210} subfacet followed by two {310} subfacets (see Fig. 1c). In this work, we will focus on three THH Rh NPs terminated by {210}, {310}, and {830} facets, respectively. In order to reasonably correspond to the experimentally observed structure and shape, all the NPs were initially constructed from a large cubic fcc single crystal. To facilitate a comparison study, the side length of the cube in each tetrahexahedron was set at $16a_0$ (a_0=3.803 Å is the lattice constant of Rh), corresponding to the particle size of 6.08 nm or so.

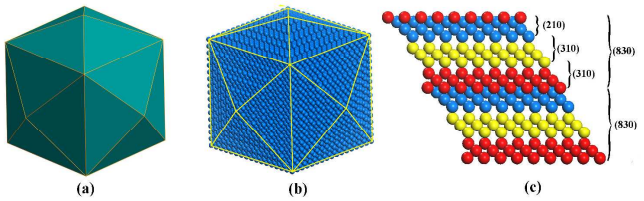

Fig. 1. (a) Schematic illustration, (b) atomic arrangement of THH Rh NP, and (c) atomic model of (830) plane that encloses the THH NP. Note that the (830) surface is composed of (210) and (310) subfacets.

In atomistic simulations, the quantum corrected Sutton-Chen (Q-SC) type many-body potentials[27] which belong to the framework of embedded-atom method (EAM)[28,29] were used to describe the interatomic interactions. According to the Q-SC potentials, the total potential energy of a system can be written as

$$U = \sum_i U_i = \sum_i \varepsilon \left[\frac{1}{2} \sum_{j \neq i} V(R_{ij}) - c\sqrt{\rho_i} \right], \quad (1)$$

in which $V(R_{ij})$ is a pair interaction function defined by the following equation

$$V(R_{ij}) = \left(\frac{a}{R_{ij}} \right)^n, \quad (2)$$

accounting for the repulsion between the i and j atomic cores; ρ_i is the electron density at ith atom site contributed by other atoms

$$\rho_i = \sum_{j \neq i} \left(\frac{a}{R_{ij}} \right)^m. \quad (3)$$

In Eqn. (1)–(3), R_{ij} is the distance between atoms i and j; a is a length parameter scaling all spacings (leading to dimensionless V and ρ); c is a dimensionless parameter scaling the attractive terms; ε sets the overall energy scale; n and m are integer parameters such that $n>m$. These parameters were optimized by fitting the lattice parameter, cohesive energy, vacancy formation energy, surface energy, bulk modulus, elastic constants and phonon dispersion, resulting in an accurate description of many properties not only for bulk materials but also for nanoscale materials.[30-35] The model parameters for Rh are given as follows: n=13, m=5, ε=2.4612 meV, c=305.499 and a=3.7984 Å.[27]

Generally, the presence of support and reactant will have an effect on the properties of nanocatalysis. However, there still lacks the accurate description of interaction between molecules in support or reactant and metallic atoms in NPs up to date. Meanwhile, in this article we address the intrinsic thermal properties of nanoparticles associated with their surface structures and shapes. Therefore, all the NPs were simulated in the vacuum environment and the influences of support or reactant on the NPs were excluded here. As the first stage of atomistic simulations, the conjugate gradient methods[36] were adopted to search the local minimum-energy configurations of all the THH Rh NPs. After the initial energy minimization, molecular dynamics (MD) methods were employed to simulate the continuous heating process. To make the simulations more realistic, the constant temperature and pressure molecular dynamics (NPT-MD) were performed to update the atomic positions and velocities. The NPs underwent the heating process consisting of a series of NPT-MD simulations from 0 to 2400 K with a temperature increment of 50 K. However, a smaller step of 10 K was adopted to investigate the shape evolution and melting behaviour more accurately at the temperature close to the critical temperature. The simulations were carried out for 200 ps of the relaxation time at each temperature, and the statistical quantities were obtained in the last 25 ps. Elaborate information concerning the thermodynamic properties and the structural characteristics of these NPs can be obtained from the output data during MD simulations. The desired temperature and ambient pressure were maintained by Nose-Hoover thermostat[37] and Berendsen approach[38], respectively. The equations of atomic motion were integrated by the Verlet-Velocity algorithm[39] with a time step of 1.0 fs.

3. Results and Discussion

It is known that the solid-liquid phase transition temperature is generally ascertained by examining the variation of thermodynamic quantities such as potential energy and specific heat capacity.[31-35, 40-43] The melting point (T_m) is usually defined as the temperature at which the heat capacity reaches its maximum. We calculated the potential energy during the heating process and then deduced the heat capacity according to following equation[40]

$$C_p(T) = \frac{dU}{dT} + \frac{3}{2}R_{gc}, \quad (4)$$

where U is the potential energy, and R_{gc}=8.314 J/molK.

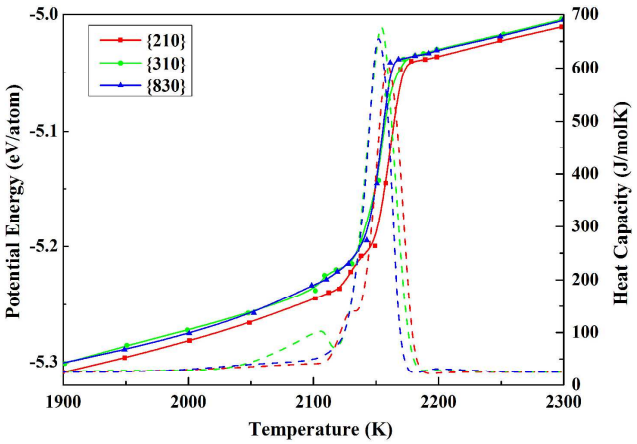

Fig. 2 Temperature dependence of potential energies and specific heat capacities of THH Rh NPs with different facets. Note that the dashed lines correspond to the heat capacity.

First, the melting process of bulk Rh has been simulated and its melting point has been proved to be about 2680 K. Clearly, the calculated melting point is 443 K (19.8%) higher than the experimental value of 2237 K [44]. Considering that crystal defects such as surface, grain boundaries and voids inevitably exist in synthesized crystalline materials, their melting processes have been experimentally proved to be heterogeneously nucleated at sites such as grain boundaries or free surfaces.[45] However, there are no free surfaces or defects in the simulated bulk crystals since three-dimensional periodic boundary conditions have been applied in the systems. The melt nucleation of surface-free perfect crystal has been verified to be homogeneous, resulting in the superheating to temperatures above its equilibrium melting point.[46] For various elemental metals, the upper limit temperature for melting in superheated crystal is about 1.2 times its equilibrium melting point.[47] Therefore, the melting point of bulk Rh, obtained by our theoretical calculations, should be reasonable although it is higher than the experimental value.

Fig. 2 illustrates the temperature-dependent potential energy and heat capacity for three THH Rh NPs. Evidently, the potential energy exhibited a linear increase with rising temperature below 2000 K, corresponding to a constant heat capacity. Note that the potential energy and heat capacity at temperatures below 1900 K are not displayed here only because they cannot provide any important information about the thermodynamic evolution of the NPs. As the temperature further increases, a sharp rise in the potential energy and accordingly a pointed peak of the heat capacity appeared at the temperature range of 2150-2160 K, indicating the occurrence of solid-liquid phase transition. After fully melted into liquid phase, the potential energy of NPs would resume a linear relationship with temperature. Note that the melting points of all Rh NPs are remarkably lower than that of bulk Rh. Generally, this reduction should be attributed to the lower surface premelting temperatures owing to the weak bonding between low-coordinated surface atoms, which has been verified by many experimental and theoretical studies.[42,43,48] Considering the approximately equal size and the same polyhedral shape of the three Rh NPs, the difference in melting points is unremarkable but still distinguishable. For example, the melting temperature of the {210} faceted NP is 10 K higher than those of the {310} and {830} faceted ones (see Fig. 2). This indicates the thermal stability of the former is slightly better than that of the latter two ones.

In order to shed light on the melting mechanism of Rh NPs, it is essential to elaborately investigate the melting processes of these NPs during continuous heating. Generally, the melting mechanism can be revealed by examining the structural change, atomic diffusion coefficients, root-mean-square displacement of atoms and so on. Currently, the Lindemann index is a simple and effective measurement in characterizing the thermodynamic evolution of a system.[49] For a system of N atoms, the local Lindemann index for the ith atom is defined as the root-mean-squared bond length fluctuation [49]

$$\delta_i = \frac{1}{N-1}\sum_{j\neq i}\frac{\sqrt{\langle R_{ij}^2\rangle - \langle R_{ij}\rangle^2}}{\langle R_{ij}\rangle}, \quad (5)$$

and the system-averaged Lindemann index is calculated as

$$\delta = \frac{1}{N}\sum_i \delta_i, \quad (6)$$

where R_{ij} is the distance between the ith and jth atoms. The Lindemann index was originally developed to study the melting behaviour of bulk crystals. The Lindemann criterion suggests that the melting occurs when the index is in the range of 0.1-0.15, depending on materials.[50] However, a smaller critical index of 0.03-0.05 was usually applied in clusters and nanoparticles owing to the relaxed restriction of surface atoms.[51]

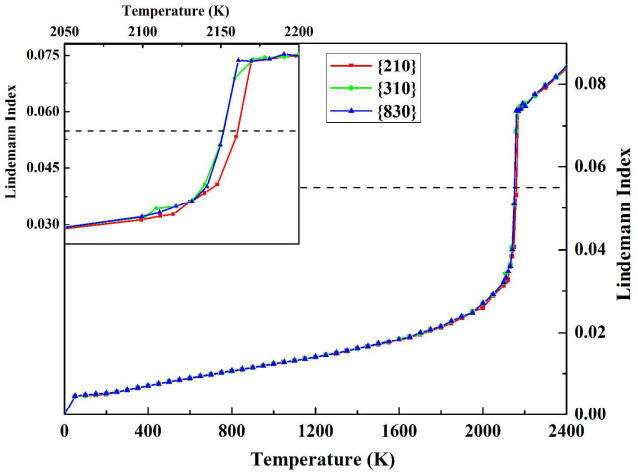

Fig. 3 Temperature-dependent Lindemann index for three THH Rh NPs during the heating process. Dashed line denotes the critical Lindemann index of 0.055. The inset highlights the sharp rise around the melting point.

The temperature dependences of Lindemann indices of three THH Rh NPs during the heating process were illustrated in Fig. 3. Analogous to the potential energy curves in Fig. 2, the Lindemann indices displayed the similar dependence on temperature. In the low temperature region, they increased linearly with the rising temperature. At about 2150 K, they began to deviate from the initially linear increase and exhibited an abrupt rise at around the melting points, corresponding to the sharp step of potential energy. Subsequently, the Lindemann indices continued to increase linearly. Generally, the critical value of the Lindemann index is dependent on the structure and constituent element of NPs. In this work, 0.055 was found to be an appropriate critical value of Lindemann index for Rh NPs by investigating the variation of Lindemann index under the heating process, as indicated by the dashed line in Fig. 3.

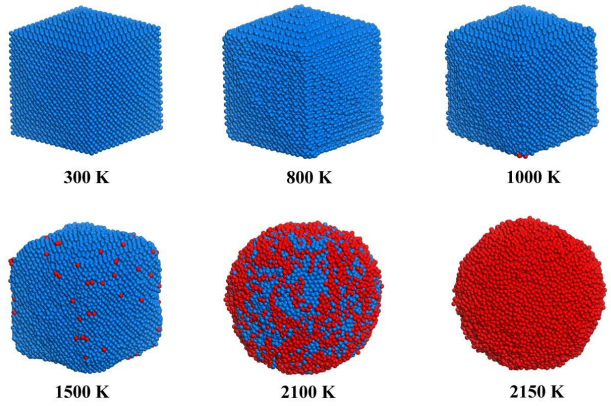

Fig. 4 Atomistic snapshots of THH Rh NPs enclosed by {830} facets taken at six representative temperatures. Coloring denotes the type of atom: dodger blue, non-Lindemann atom; red, Lindemann atom.

In order to visualize the melting process, we extracted the coordinates of all atoms in the Rh NPs at different temperatures. As a representative, Fig. 4 demonstrates the atomistic snapshots of {830} faceted THH NP taken at six typical temperatures. Similar to the study of melting for a surface-free Lennard-Jones crystal,[46] the concept of Lindemann atom was introduced here: An atom whose Lindemann index exceeds the critical value is defined as Lindeamnn atom; otherwise, it is marked as non-Lindemann atom. As shown in Fig. 4, Rh NP can maintain its initial morphology and surface structure well at room temperature of 300 K. At around 800 K, those atoms at eight corners, whose coordination number (CN) is 3, diffused inward firstly, while the atoms at six apexes (CN=4) remained at their initial positions, suggesting that the low-coordinated atoms migrated easily with the rising temperature. At this time, the THH shape and associated surface structure can still be preserved well. With the temperature further increasing, other low-coordinated atoms (typically CN=5 and 6) on the surface also began to diffuse. When the temperature went up to 1100 K, some of atoms on the edge had already migrated from their initial sites, while the shape of THH was still preserved since the atomic step can be distinguishable. Further heating drove the diffusion of more surface atoms, resulting in the destruction of surface structure. At 1500 K, the THH shape became obtuse since the {830} facets cannot be discernible. One can find that the THH NP had transformed into a sphere-like one at 2100 K. At this time, surface atomic arrangements were completely disordered and a large number of Lindemann atoms appeared on the surface, indicating the initiation of surface premelting. As the temperature was increased to 2150 K, all the surface atoms had all turned into Lindemann atoms, suggesting that the premelting had extended over the whole surface and spread into the interior region progressively. A further increasing temperature resulted in the overall melting of THH NP and the formation of a liquid NP. An analogous evolution progress was also found in {210} and {310} faceted THH NPs.

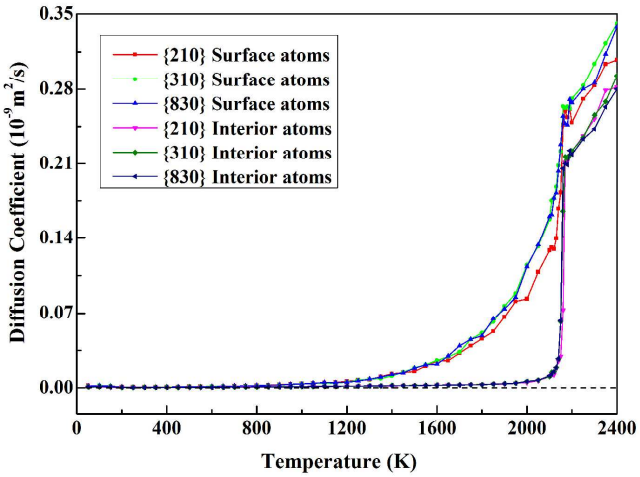

Fig. 5 Diffusion coefficients of surface and interior atoms as a function of temperature.

Besides the thermal evolution of THH Rh NPs under continuous heating, as discussed above, the diffusive behavior of atom is also a crucial issue that should be clarified due to its technological significance for application in catalysis.[52] For example, atomic redistribution in NPs can be achieved through the diffusion process, thus changing their configurations and finally affecting their catalytic performance. Furthermore, an investigation on the diffusion process is instructive to understand the dynamic evolution of

microstructure. Generally, the thermally driven diffusion is characterized by the diffusion coefficient which can be calculated from the mean-square displacement (MSD) of individual atom by the following equation [53]

$$D = \frac{1}{2dNt}\sum_{i=1}^{N}[r_i(t) - r_i(0)]^2 , \quad (7)$$

where d and N are the dimensionality and the total number of atoms in a system, respectively; t is the time interval in the simulation, $r_i(0)$ is the original position of atom i for t=0, $r_i(t)$ is its current position. In order to highlight the atomic diffusion behaviour, all atoms were classified into two categories according to their CNs: An atom whose CN is less than twelve was regarded as surface atom, otherwise as interior atom. The temperature-dependent diffusion coefficients for surface atoms and interior atoms were illustrated in Fig. 5. The curves of the three NPs seemed to be basically similar. At the initial stage of heating (typical below 800 K), the diffusive ability of atoms was insufficient although the potential energy linearly increased with rising temperature. Therefore, all atoms could only vibrate around their equilibrium positions, and the diffusion coefficients of both interior and surface atoms were very small, as illustrated in Fig. 5. When the temperature exceeded 800 K, the diffusion coefficient of surface atoms increased progressively, while that of interior ones kept invariant. Furthermore, it can be observed that surface atomic diffusion coefficient of {210} faceted NP was lower than those of {310} and {830} faceted NPs, indicating that surface structure of {210} faceted NP may be transformed more slowly than those of the other two ones. The internal atoms did not migrate from their original positions until the temperature reached 1600 K or so. Afterwards, the diffusion coefficient of interior atoms began to increase. When the temperature was close to the melting point, the diffusivities of both surface and interior atoms exhibited a sharp rise, indicating a first order phase transition from solid to liquid.

As is known, surface structure of NPs plays key roles during catalytic processes because catalytic reactions preferentially occur at surface.[26] Owing to the fact that the destruction of high-index facets would lower the catalytic activities of THH NPs, the examination of the transformation temperature of surface structure is crucial for both the design and application of NP catalysts. Note that the shape of NP is determined by its surface structure, thus the shape change is indicative of surface structure transformation. To accurately describe the shape change, here we introduce the shape factor as follows[54]

$$S = \frac{1}{R^2}\sqrt{\frac{1}{\mathrm{N}}\sum_{i=1}^{N}(r_i^2 - R^2)^2} , \quad (8)$$

in which r_i is the distance from the ith atom to the particle center of mass and R is the root-mean-square of r_i,

$$R = \sqrt{\frac{1}{\mathrm{N}}\sum_{i=1}^{N} r_i^2} . \quad (9)$$

According to the definition above, the shape factor is a sensitive indicator of particle shape, independent on the total atomic number N. Fig. 6 illustrates the temperature dependent shape factors for the three THH Rh NPs.

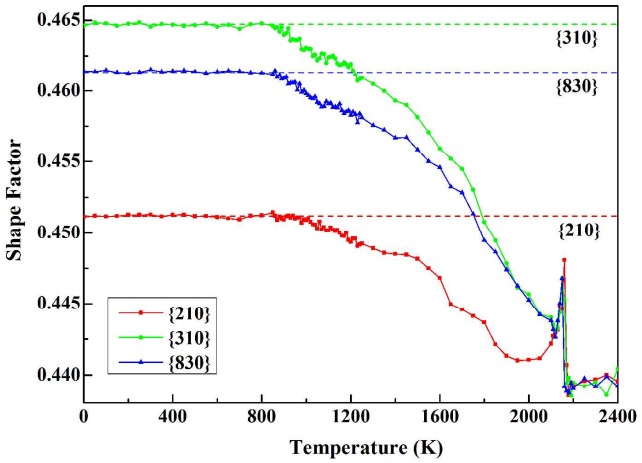

Fig. 6 Temperature-dependent shape factors of different high-index-faceted THH Rh NPs. Dashed line indicates the initial value at low temperatures.

Apparently, different high-index-faceted THH correspond to different initial values of S, as indicated by the dashed lines in Fig. 6. At the low temperature region, each NP can retain its original shape, and no observable change of surface structure occurred because of small diffusivity of surface atoms, in accord with the atomistic snapshots in Fig. 4. When the temperature was beyond 1000 K, all the shape factors began to deviate from their initial values to different extent, suggesting a noticeable change of surface structure and the initialization of shape transformation.

According to Fig. 6, the critical temperature at which the shape factor began to continuously decrease was ascertained to be 1000, 920, 910 K for the THH NPs enclosed by {210}, {310}, {830} facets, respectively. It is worth pointing out that the shape transformation temperature of the THH NP is remarkably lower than its melting point, implying the shape transformation occurred much earlier than the melting. Moreover, these critical temperatures were also consistent with their corresponding diffusion efficient of surface atoms. For example, the {210} faceted NP with the highest shape transformation temperature possessed the lowest diffusivity of surface atoms among the three NPs. Besides, the {310} and {830} faceted NPs exhibited close critical temperatures since their diffusion coefficients were almost identical (see Fig. 5). By analysis of bond, it is found that the average CN of surface atoms was 8.455, 8.263, and 8.294 for the {210}, {310}, and {830} faceted NPs, respectively. Therefore, it is expected that higher CN of surface atoms leads to lower surface diffusivity, thus being beneficial to enhancing the shape stability. Furthermore, the {210} faceted NP was closer to spherical shape in comparison with the other two THH NPs (see Fig. 6). Note that the shape factor is 0.44 for ideal sphere NP. Nevertheless, the shape factors of different THH NPs finally converged to the same value at high temperatures, indicating that all the NPs were evolved into the same shape after completely melting.

From above discussion, one can find that the thermodynamic and shape stability of {310} and {830} faceted NPs were almost identical, and both of them were worse than {210} faceted one. Considering that the {830} facet is composed of {210} and {310} subfacets, the stability of high-index faceted NP is dominated by the {310} subfacet which possesses worse stability. Moreover, this

regularity could be expected to extend to those NPs with other high-index facets.

4. Conclusions

In summary, we employed MD simulations to investigate the thermodynamic stability and shape evolution of THH Rh NPs with high-index facets. The Lindemann index, diffusion coefficient, and shape factor were adopted to explore the melting behavior and shape transformation of these NPs during continuous heating. The results reveal that both the thermal and shape stabilities of {210} faceted NP are better than those of {310} and {830} faceted NPs. Moreover, the shape transformation temperatures of these NPs are much lower than their melting points. Further analyses discover that higher CN of surface atoms leads to lower surface diffusivity, thus being beneficial to enhancing the thermal and shape stabilities. Since the {830} plane is comprised of {210} and {310} ones, the stability of {830} faceted NP is mainly governed by the {310} subfacet which has relatively poor stability. This regularity could be extended to other high-index-faceted metallic NPs. Our study provides an in-depth understanding of thermodynamic evolution of high-index-faceted Rh NPs, which is expected to have important implications not only to the exploitation of metallic NPs with high catalytic activity but also to the design of novel nanostructures.

Acknowledgements

This work is supported by the National Natural Science Foundation of China (Grant Nos. 51271156, 11474234 and 11204252), the Natural Science Foundation of Fujian Province of China (Grant No. 2013J06002), and the Specialized Research Fund for the Doctoral Program of Higher Education of China (Grant No. 20130121110012).

Notes and references

* E-mail: yhwen@xmu.edu.cn, huangrao@xmu.edu.cn.
Phone: (+86) 592-218-2248. Fax: (+86) 592-218-9426.
[a] Institute of Theoretical Physics and Astrophysics, Department of Physics, Xiamen University, Xiamen 361005, China
[b] State Key Laboratory of Physical Chemistry of Solid Surfaces, Department of Chemistry, Xiamen University, Xiamen 361005, China

1 Y. W. Zhang, M. E. Grass, W. Y. Huang and G. A. Somorjai, *Langmuir*, 2010, **26**, 16463.
2 H. S. Gandbi, G. W. Graham and R. W. McCabe, *J. Catal.*, 2003, **216**, 433.
3 Y. Zhang, M. Janyasupab, C. W. Liu, X. Li, J. Xu and C. C. Liu, *Adv. Funct. Mater.*, 2012, **22**, 3570.
4 J. L. Pellegatta, C. Blandy, V. Colliere, R. Choulkroun, B. Choudret, P. Cheng and K. Philppot, *J. Mol. Catal. A: Chem.*, 2002, **178**, 55.
5 Z. L. Wang, *J. Phys. Chem. B*, 2000, **104**, 1153.
6 R. Narayanan and M. A. El–Sayed, *Nano Lett.*, 2004, **4**, 1343.
7 H. Lee, S. E. Habas, S. Kweskin, D. Butcher, G. A. Somorjai and P. Yang, *Angew. Chem. Int. Ed.*, 2006, **118**, 7988.
8 K. M. Bratlie, H. Lee, K. Komvopoulos, P. Yang and G. A. Somorjai, *Nano Lett.*, 2007, **7**, 3097.
9 C. K. Tsung, J. N. Kuhn, W. Y. Huang, C. Aliaga, L. I. Hung, G. A. Somorjai and P. Yang, *J. Am. Chem. Soc.*, 2009, **131**, 5816.
10 G. A. Bernasek Somorjai, *Surf. Sci.*, 1975, **48**, 204.
11 N. P. Lebedeva, M. T. M. Koper, J. M. Feliu, R. A. van Santen, *J. Phys. Chem. B*, 2002, **106**, 12938.
12 Y. D. Yin and A. P. Alivisatos, *Nature*, 2005, **437**, 664.
13 N. Tian, Z. Y. Zhou, S. G. Sun, Y. Ding and Z. L.Wang, *Science*, 2007, **316**, 732.
14 Z. Y. Zhou, Z. Z. Huang, D. J. Chen, Q. Wang, N. Tian and S. G. Sun, *Angew. Chem. Int. Ed.*, 2010, **49**, 411.
15 T. Ming, W. Feng, Q. Tang, F. Wang, L. D. Sun, J. F. Wang and C. H. Yan, *J. Am. Chem. Soc.*, 2009, **131**, 16350.
16 J. Li, L. H. Wang, L. Liu, L. Guo, X. D. Han and Z. Zhang, *Chem. Commun.*, 2010, **46**, 5109.
17 N. Tian, Z. Y. Zhou, N. F. Yu, L. Y. Wang and S. G. Sun, *J. Am. Chem. Soc.*, 2010, **132**, 7580.
18 C. L. Lu, K. S. Prasad, H. L. Wu, J. A. Ho and M. H. Huang, *J. Am. Chem. Soc.*, 2010, **132**, 14546.
19 Y. J. Deng, N. Tian, Z. Y. Zhou, R. Huang, Z. L. Liu, J. Xiao and S. G. Sun, *Chem. Sci.*, 2012, **3**, 1157.
20 J. D. Hoefelmeyer, K. Niesz, G. A. Somorjai and T. D. Tilley, *Nano Lett.*, 2005, **5**, 435.
21 S. M. Humphrey, M. E. Grass, S. E. Habas, K. Niesz, G. A. Somorjai and T. D. Tilley, *Nano Lett.*, 2007, **7**, 785.
22 Y. W. Zhang, M. E. Grass, J. N. Kuhn, F. Tao, S. E. Habas, W. Y. Huang, P. D. Yang and G. A. Somorjai, *J. Am. Chem. Soc.*, 2008, **130**, 5868.
23 N. Zettsu, J. M. McLellan, B. Wiley, Y. D. Yin, Z. Y. Li and Y. N. Xia, *Angew. Chem. Int. Ed.*, 2006, **45**, 1288.
24 N. F. Yu, N. Tian, Z. Y. Zhou, L. Huang, J. Xiao, Y. H. Wen and S. G. Sun, *Angew. Chem. Int. Ed.*, 2014, **53**, 5097.
25 J. M. Sun, D. Ma, H. Zhang, X. M. Liu, X. W. Han, X. H. Bao, G. Weinberg, N. Pfaender and D. S. Su, *J. Am. Chem. Soc.*, 2006, **128**, 15756.
26 R. Ferrando, J. Jellinek and R. L. Johnston, *Chem. Rev.*, 2008, **108**, 846.
27 T. Cagin, Y. Kimura, Y. Qi, H. Li, H. Ikeda, W. L. Johnson and W. A. Goddard, *Mater. Res. Soc. Symp. Proc.*, 1999, **554**, 43.
28 M. I. Daw Baskes, *Phys. Rev. Lett.*, 1983, **50**, 1285.
29 M. S. Daw, M. I. Baskes, *Phys. Rev. B*, 1984, **29**, 6443.
30 H. Ikeda, Y. Qi, T. Cagin, K. Samwer, W. L. Johnson and W. A. Goddard, *Phys. Rev. Lett.*, 1999, **82**, 2900.
31 S. K. R. S. Sankaranarayanan, V. R. Bhethanabotla and B. Joseph, *Phys. Rev. B*, 2005, **72**, 195405.
32 Y. H. Wen, Y. Zhang, J. C. Zheng, Z. Z. Zhu and S. G. Sun, *J. Phys. Chem. C*, 2009, **113**, 20611.
33 R. Huang, Y. H. Wen, Z. Z. Zhu and S. G. Sun, *J. Mater. Chem.*, 2011, **21**, 11578.
34 R. Huang, Y. H. Wen, Z. Z. Zhu and S. G. Sun, *J. Phys. Chem. C*, 2012, **116**, 8664.
35 Y. H. Wen, R. Huang, C. Li, Z. Z. Zhu and S. G. Sun, *J. Mater. Chem.*, 2012, **22**, 7380.
36 A. R. Leach, *Molecular Modelling: Principles and Applications*, Prentice–Hall: London, 2001.
37 D. J. Evans and B. L. Holian, *J. Chem. Phys.*, 1985, **83**, 4069.
38 H. J. C. Berendsen, J. P. M. Postma, W. F. van Gunsteren, A. DiNola and J. R. Haak, *J. Chem. Phys.*, 1984, **81**, 3684.

39 W. C. Swope, H. C. Andersen, P. H. Berens and K. R. Wilson, *J. Chem. Phys.*, 1982, **76**, 637.
40 Y. Qi, T. Cagin, W. L. Johnson and W. A. Goddard, *J. Chem. Phys.*, 2001, **115**, 385.
41 X. M. Zeng, R. Huang, G. F. Shao, Y. H. Wen and S. G. Sun, *J. Mater. Chem. A*, 2014, **2**, 11480.
42 G. A. Breaux, C. M. Neal, B. Cao and M. F. Jarrold, *Phys. Rev. Lett.*, 2005, **94**, 173401.
43 J. Kang, S. H. Wei and Y. H. Kim, *J. Am. Chem. Soc.*, 2010, **132**, 18287.
44 A. M. James and M. P. Lord, *Macmillan's Chemical and Physical Data*, Macmillan: London, 1992.
45 R. W. Cahn, *Nature*, 1986, **323**, 668.
46 Z. H. Jin, P. Gumbsch, K. Lu and E. Ma, *Phys. Rev. Lett.*, 2001, **87**, 055703.
47 K. Lu and Y. Li, *Phys. Rev. Lett.*, 1998, **80**, 4474.
48 Q. S. Mei and K. Lu, *Prog. Mater. Sci.* 2007, **52**, 1175.
49 Y. Shibuta and T. Suzuki, *Chem. Phys. Lett.*, 2007, **445**, 265.
50 H. Lowen, *Phys. Rep.*, 1994, **237**, 249.
51 Y. Q. Zhou, M. Karplus, K. D. Ball and R. S. Berry, *J. Chem. Phys.*, 2002, **116**, 2323.
52 J. Yang and J. Y. Ying, *J. Am. Chem. Soc.*, 2010, **132**, 2114.
53 S. J. Plimpton and E. D. Wolf, *Phys. Rev. B*, 1990, **41**, 2712.
54 Z. L. Wang, Y. Q. Zhong and S. Y. Wang, *Text. Res. J.* 2012, **82**, 454.

Graphical Abstract

Atomistic simulations are used to investigate the thermodynamic and shape stability of tetrahexahedral Rh nanoparticles with high-index facets.